15

# Large area multi-element single-photon detector

© M.D. Soldatenkova,[1,2] A.I. Lomakin,[2] S.S. Svyatodukh,[1,2,4] N.A. Titova,[2] E.M. Baeva,[1,2] A.I. Kolbatova,[2] G.N. Goltsman[1,2,3,4]

[1] National Research University Higher School of Economics,
109028 Moscow, Russia
[2] Moscow Pedagogical State University,
119991 Moscow, Russia
[3] Russian Quantum Center,
121205 Moscow, Russia
[4] LLC „Superconducting nanotechnology“,
115114 Moscow, Russia
e-mail: msoldatenkova@hse.ru

*Received April 22, 2025*
*Revised April 22, 2025*
*Accepted April 22, 2025*

New applications of superconducting single-photon detectors increase the requirement for large active area detectors. In this study we designed and fabricated a 12-pixel NbN detector with a large active area and a stripe width of 500 nm and an active area size of $45 \times 50\,\mu$m, which is suitable for matching with multimode optical fiber. We investigated the current-voltage characteristics and determined the critical current $I_c$ of the sample. This value was compared with the maximum possible theoretical value of the depairing current $I_{dep}$. Due to the design of the multi-element NbN detector, which eliminates the influence of the current bunching effect, most of the studied samples demonstrate $I_c/I_{dep}$ value exceeding 0.7. Our results indicate that most of the pixels on the studied multi-element detector are capable of single photon detection.

**Keywords:** superconducting single-photon detectors, superconductivity, critical current of a superconductor, shunt resistor, volt-ampere characteristics.

DOI: 10.61011/TP.2025.09.61857.68-25

## Introduction

Superconducting nanowire single-photon detectors (SNSPD), which are manufactured based on a narrow superconducting stripe (the width is about 100 nm) bent as a meander for better matching with the optical fiber and designed to operate in the visible and the IR range are in great demand in various fields of quantum technologies [1,2]. Due to detection efficiency close to unity, the time jitter $< 10$ ps [3,4], low restoration time and a low dark count rate [5], the SNSPDs have no analogues in terms of sensitivity for detecting even weak optical signals. It makes them indispensable for quantum processing of information and implementing optical communication channels by means of an optical fiber and in open space. For example, the study [6] demonstrates a system of quantum key distribution via a fiber communication line over the distance of 830 km. However, the standard SNSPD usually has an active area of the diameter of $15\,\mu$m and less for matching with the single-mode optical fiber.

At the same time, the detectors that have the large detecting active area are in great demand for experiments related to searching dark matter [7], confocal fluorescence microscopy [8], the LIDAR technology (Light Detection and Ranging) [9] as well as studying deep space [10]. The biggest SNSPD single pixel has a size of about $400 \times 400\,\mu$m [5]. However, great kinetic inductance prevents further advancement of the active area of the single-pixel SNSPD [11]. This requirement resulted in creation of fast detectors that consist of several shorter SNSPDs, which are arranged in one chip and connected in parallel. It allowed reducing kinetic inductance and increasing the detector rate above $10^9$ cps (counts per second). These devices are exemplified in the studies [10,12–18]. However, such detectors occupy a quite small area of about $100-400\,\mu\text{m}^2$ and, most importantly, they have a low filling factor, i.e. the detecting acting area of the device is significantly less than an area occupied by the entire device [19]. Thus, for example, a study has been done quite recently to demonstrate the fast detector that occupies the large area $320-320\,\mu$m and is based on amorphous superconducting WSi SNSPDs of the width of160 nm each, for deep space research, but the filling factor turns out to be less than 15 % [10]. Besides, the narrow SNSPD stripes are usually manufactured using electron-beam lithography, which is characterized by low performance of the samples with high characteristics. It should be noted that in order to solve tasks that require overlapping of a large area, for example, for matching with a multi-mode fiber or a lens, it is worth considering other ways of development.

A new approach to creating the large-area detector is to use the superconducting detector with a micron-wide

stripe (SMSPD, Superconducting microwire single-photon detector). Detectability of single photons by SMSPD was theoretically predicted in 2017 within the framework of a new model created for describing a single-photon response of SNSPD: „Models of a superconducting vortex generated by a photon“ [20]. A key element of this model is a theory of origination of the superconducting vortex due to current crowding at sides of the hot spot. When a bias current is above a certain threshold value, the vortices can separate from the hot spot and pass in an avalanche-like manner through the superconducting stripe, causing dissipation and a growth of the hot spot. This mechanism of the single-photon response was experimentally demonstrated in the study [21]. This study has investigated the response in NbN bridges, whose width significantly exceeded the area of the hot spot — more than 150 nm. Thus, only origination of the vortices can explain the single-photon response in the wide bridges. The most important step was reduction of kinetic inductance of each element due to increasing the width of nanowire. This paved the way for creation of the detector that not only occupies the large area, but also has a higher filling coefficient (the large detecting region). It has been recently demonstrated that SMSPD single pixel can cover the area of $1\,\text{mm}^2$ with the filling coefficient from 0.3 to 0.5 [22]. It is important to note that such detectors already demonstrate saturation of detection efficiency and have proven themselves as promising and functional devices [23] which have significant potential in practical applications.

Despite the above-listed advantages of the SMSPD, it is necessary to take into account a number of specific features of operability of the device. Thus, for example, significant increase of the stripe width results in reduction of kinetic inductance detector, thereby resulting in origination of a latching effect. It is a phenomenon, in which a normal domain that is formed in a place where the photon is absorbed, has not enough time to decrease and restore the superconducting state which causes a detector's inability to record to next photons [24]. The latching effect can be eliminated by adding either serial inductance or parallel resistance Rsh [22]. It is known that by theoretically and experimentally studying a dynamic mechanism of slip of the order parameter phase in superconducting ultrathin nanowires (12–18 nm) in the presence of a shunt resistor in the study [25], the authors have assumed that $I_c$ can be controllably approximated very closely to $I_{dep}$ by transmitting the current through the shunt-resistor detector. However, the present of the shunt degrades time characteristics of the detector. Besides, according to the theoretical study of D.Yu. Vodolazov [20], the most important condition for efficient operation of the superconducting single-photon detector with the micron-wide stripe is fulfillment of the ratio $I_c/I_{dep} > 0.7$, where $I_{dep}$ is a theoretical depairing current of copper pairs for a specific material and structure, while $I_c$ is an experimentally-obtained value of the critical current. The theory predicts that if the value of the critical current is close to the depairing current, then detectability of the photons does not depend on the detector width. However, in the experiment the magnitude $I_c$ rarely reaches the maximum possible current $I_{dep}$. The value of the critical current turns out to be very sensitive to defects in the superconductors. Thus, for example, various defects (pinning centers) can include natural defects in a material (non-superconducting nanoparticles) or technological specific features of structuring. In addition to properties of the superconducting films, achievability of the maximum value of the critical current is also largely affected by selection of a topology of the detector. The most suitable for this task is a superconducting microbridge, since this structure has no turns, which result in suppression of the critical current that originates due to the current crowding effect when flowing over obstacles [26]. In addition, in order to successfully detect single photons, it is required that the material has high resistivity in a normal state. The study [27] has experimentally investigated a dependence of light counts of the SMSPD on the bias current for the samples with a different value of resistance per square $R_s$. The detectors that have a large value of resistance per square $R_s$ (more than $630\,\Omega$/sq) have demonstrated detectability of single photons with lower bias currents than the detectors with the lesser value of $R_s$. Thus, in order to create the high-efficiency working SMSPD, it is necessary to take into account many technological aspects.

In the present study, the authors have designed a multi-element NbN detector with the large active area and the filling factor of 0.7, manufactured it and investigated volt-ampere characteristics of the produced device. The detector is manufactured based on a highly-resistant NbN film ($R_s = 980\,\Omega$/sq). The one chip includes 12 SMSPD sample with the stripe width of 500 nm. The active area size of the device is $45 \times 50\,\mu$m, which is suitable for matching with the multi-mode optical fiber. In order to prevent the latching effect, we have installed the resistor $R_{sh} = 33\,\Omega$ in parallel to each element and measured the volt-ampere characteristics for the eight samples in a helium closed-loop cryorefrigerator at the temperature of 2.7 K. The volt-ampere characteristics were studied to show that depending on residual resistance of the sample the measured critical current could turn out to be overestimated due to distribution of the current between sample and the shunt resistance. Based on the volt-ampere characteristics, we have determined the real critical current $I_c$ of the sample and compared it with the depairing current. Due to the design of the multi-element NbN detector, which excludes the influence of the current crowding effect on the total critical current of the stripe, the value of $I_c(T)/I_{dep}(T)$ in the most studied samples exceeds 0.7. The obtained results show that our large area multi-element detector has an advantage in the filling factor as compared to the large-area SNSPD-based detectors and has a big potential for further work dedicated to designing the large-area multi-element detector.

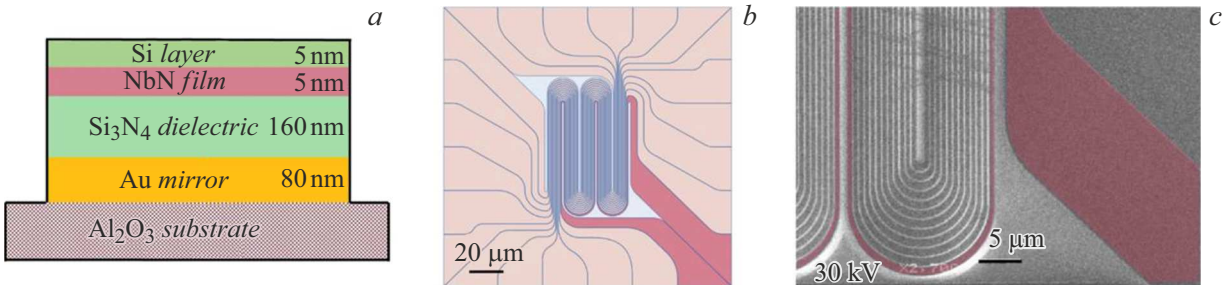


**Figure 1.** *a* — a schematic sequence of the layers of the studied device. From top to bottom: the passivating silicon layer Si — 5 nm, the superconducting NbN film — 5 nm, the $Si_3N_4$ film — 160 nm, the Au film — 80 nm, the $Al_2O_3$sapphire substrate; *b* — the sketch of a design of the central part of the multi-element detector; *c* —the image of the finished multi-element detector, which is obtained by means the scanning electron microscope. The red color marks one of the 12 elements of the detector.

## 1. Manufacturing of the detectors

The studied detector was manufactured from the NbN film of the thickness of 5 nm, which was grown by means of reactive magnetron sputtering in the installtion AJA Orion-8. The sputtering installation was pre-vacuumed to $3 \cdot 10^{-8}$ Torr. A Nb target (with purity of 9.9999) was sputtered in the Ar:$N_2$ atmosphere at the pressure of 3.5 mTorr. In order to improve absorption of the photons with the wavelength of 1550 nm, the film was deposited to the sapphire substrate ($r$-cut) with golden signs and mirrors of the thickness of 80 nm, which were pre-prepared on it. Then, the golden layer was coated with the $Si_3N_4$ dielectric of the thickness 160 nm, which was produced by plasma-enhanced chemical vapor deposition (PECVD). Adhesion of the deposited NbN film was improved by heating the substrate to 350 °C. After deposition, the film was passivated with the 5 nm-layer of silicon *in situ*. The silicon film deposited above NbN is completely removed in the region of contact areas to ensure good contact to the superconducting material, wherein in region of the detecting part the silicon layer remains, thereby preventing oxidation of NbN. The deposited NbN-film had the temperature of the superconducting junction ($T_c = 7.2$ K), the surface resistance $R_s$ at the room temperature (804 Ω/sq) and the residual resistance ratio ($RRR = 0.79$). The schematic sequence of the layers is shown in Fig. 1, *a*.

The multi-element detector designed using the PHIDL library is shown in Fig. 1, *b*. The device consists of 12 separate superconducting stripes that form the active area of the size of $45 \times 50\,\mu$m. The width of each stripe in this area is 500 nm, while a distance between the adjacent stripes is 200 nm. In order to prevent the current crowding effect, the minimum internal bending radius of the stripe is $1\,\mu$m. In the bending location the width of the stripe smoothly increases to $1\,\mu$m and returns to the initial width in the active area. When designing, we also abandon an earthing island that is common for all the stripes, which is arranged in the chip (using the common earthing island is exemplified in the studied [15–17,19]). Despite the fact that this solution somewhat increases duration of SMSPD manufacturing by means of electron-beam lithography, it can minimize the current crowding effect that originates when the current goes from the stripe into the earthing island. The stripes are designed so as to have approximately equal kinetic inductance $L_K$. The NbN film was structured in accordance with the developed design in three stages. The first stage included formation of the SMSPD stripe by means of electron-beam lithography and plasma-enhanced chemical etching in a mixture of the gases Ar and $SF_6$. At this stage, a mask was the positive electron-beam resist PMMA 3 %. The second stage included formation of windows of contact islands to the stripes. The Ti/Au contact metallization was deposited by thermal evaporation through the mask of the positive photoresist Az1512. The excess metallization were removed after deposition during *lift-off*. The third stage included formation of the protective mask by means of electron-beam lithography in the negative electron-beam resist maN-2405 for the central part of the structures. After formation of the protective mask, plasma-enhanced chemical etching of the NbN film was carried out as per a field in order to create a finite topology of the multi-element detector. An image of the finished multi-element superconducting detector, which is obtained by means of the scanning electron microscope, is shown in Fig. 1, *c*. After etching, the protective mask was removed in warm acetone and the plate was divided into separate chips. After structuring, resistance of each stripe is about 600 kΩ at the temperature of 300 K. For each detector element, the number of the squares $N$ is about 610. Thus, resistance per square of the film $R_s$ is about 980 Ω/sq at 300 K.

## 2. Experimental methods

The finished detectors were studied in the Gifford-McMahon cryorefrigerator at the basic temperature of 2.7 K in two stages by measuring the dependence of resistance on the temperature and investigating the volt-ampere characteristics. The universal bias unit Scontel ControlUnit (3 generation) is used as a voltage source that has measurement devices - a voltmeter and ammeter, built-in amplifiers and a bias tee. The installation scheme is

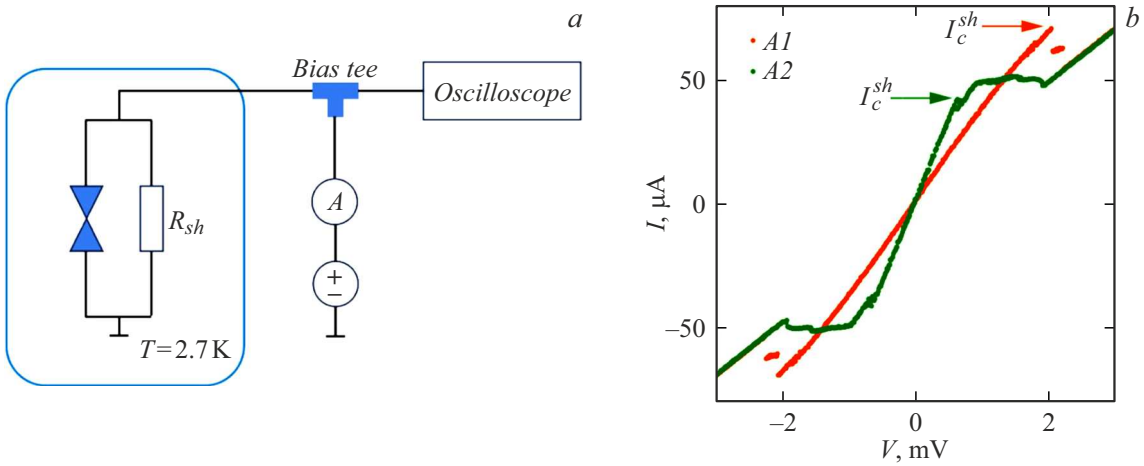


**Figure 2.** *a* — a measurement diagram of the volt-ampere characteristics. The shunt resistance $R_{sh} = 33\,\Omega$ is installed in parallel to each detector. The measurements are carried out at the temperature $T = 2.7\,\text{K}$; *b* — the volt-ampere characteristics for the samples. *A1* and *A2* — the orange and green curves, respectively, which are obtained in a voltage-stabilization mode. For the sample *A1* the residual resistance is 20 Ω, while for the sample *A2* the residual resistance is 1.4 Ω.

shown in Fig. 2, *a*. An output of the unit was connected via the bias tee to an oscilloscope for detecting electrical interference in the system. The device can operate both in the current-stabilization mode and the voltage-stabilization mode. The dependence of the resistance on the temperature was measured using the 370 AC Resistance Bridge and the LakeShore 218 temperature monitor with calibration for the diode thermometer. The resistance of the samples was tested at the room temperature by using a manual probe station.

## 3. Study of the temperature dependence of the resistance

Before low-temperature measurements in the closed-loop cryostat, the samples were tested in the TS 200 probe station. Using probe heads, a two-point measurement diagram was taken to obtain the resistance values at the room temperature for all the samples on the chip. The values were 582–612 kΩ. Besides, it was checked to make sure if there are short-circuiting jumpers to the mirror or between the adjacent detectors. Then we studied the sample in liquid helium and obtained the dependence of the resistance on the temperature (Fig. 3).

The black arrow marks the temperature of transition of the sample into the superconducting state $T_c$, which was 7.1 K and determined as a temperature at which $R = R_n/2$, where $R_n$ is normal resistance of the superconductor, which is equal to 724 kΩ, which corresponds to $R_s = 1200\,\Omega/\text{sq}$ at 20 K. The obtained value of the critical temperature is important for further understanding of principles of operation of the detector and for evaluating the value of the depairing current.

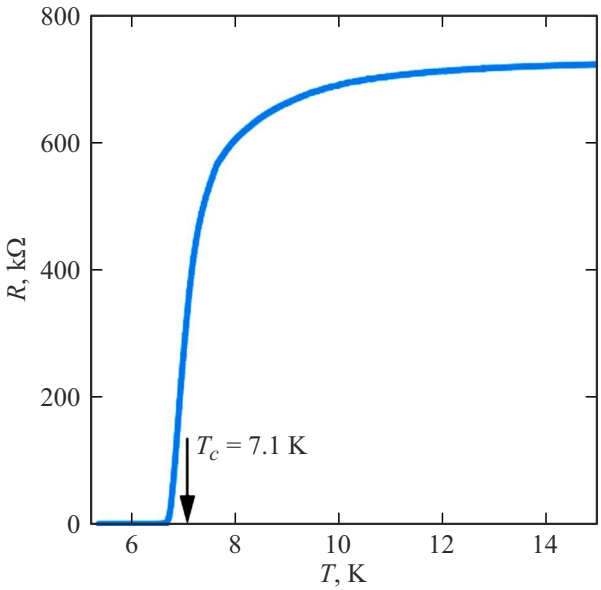


**Figure 3.** Dependence of the resistance $R$ on the temperature $T$. $R_n = 723\,\text{k}\Omega$ is normal resistance of the superconductor. The critical superconducting transition temperature $T_c$ is 7.1 K and corresponds to $R_n/2$, it is marked by the black arrow on the graph.

## 4. Evaluation of the value of the depairing current

In order to evaluate the value of the depairing current, we use an expression from the study [28]:

$$I_{dep}(T) = 0.74w\,\frac{\Delta(0)^{3/2}}{eR_s\sqrt{\hbar D}}\left(1-(T/T_c)^2\right)^{3/2}, \qquad (1)$$

where $\Delta(0) = 1.764kT_c$ — the energy of a superconducting slit, $e$ — the charge of the electron, $D = 0.5\,\text{cm}^2/\text{s}$ — the

typical value of the diffusion constant for the NbN-film [29], $w = 500\,\text{nm}$ — the width of the unit superconducting detector, $R_s = 980\,\Omega/\text{sq}$ — the resistance per square at the temperature of 300 K, $T = 2.7\,\text{K}$ — the basic temperature of the measurements, $T_c = 7.1\,\text{K}$ — the critical superconducting transition temperature that is obtained from the dependence of the resistance on the temperature. Using the expression (1), we obtain that the expected value of the depairing current for these samples is $58.8\,\mu\text{A}$ at the temperature of 2.7 K.

## 5. Discussion of the volt-ampere characteristics

8 stripes of 12 were selected to characterize the chip (the samples A1-A8). The chip with the samples was placed on a holder with a circuit board, which included twelve 50-Ohm lines with common earthing. Each stripe was connected to its coplanar line to supply voltage or current to the stripe. Each sample is biased by the current or voltage in the two-point diagram, read separately and has its own shunt resistor that is connected to the coplanar line and common earthing. The diagram for measuring the volt-ampere characteristics in the voltage-stabilization mode is shown in Fig. 2, *a*. Let us consider the typical volt-ampere characteristics for the samples *A1* and *A2*, which are shown in Fig. 2, *b*. For the sample *A1*, the dependence is shown by the orange curve, while for the sample *A2* it is shown by the green curve. The black arrow marks the value of the measured critical current of the sample $I_c^{sh}$ that is in parallel connection with the shunt resistor. It should be noted that in the present study we have not selected an optimal value of $R_{sh}$ to eliminate the latching effect, as done, for example, in the study [27], but just investigated its effect on the volt-ampere characteristics. A slope of the volt-ampere characteristic at zero bias voltage corresponds to a sum of resistances of wires, resistance in the bias tee and resistance that is determined by parallel connection of residual resistance $R_p$ of the sample and shunt resistance $R_{sh}$. From the slope of the volt-ampere characteristics we have obtained the values of the residual resistances $R_p$, which are 20 and $1.4\,\Omega$ for *A1* and *A2*, respectively. It can be noted from Fig. 3, *b* that the sample *A1* with higher residual resistance has the higher critical current $I_c^{sh} = 71.4\,\mu\text{A}$ as compared to the sample *A2* that has $I_c^{sh} = 43\,\mu\text{A}$. It is obvious that the value of the critical current can not exceed the value $I_{dep} = 58.8\,\mu\text{A}$ and this observation can be interpreted as follows. Since each sample is shunted with the resistor with the resistance $R_{sh}$, the total current is redistributed between the shunt and residual resistances as follows:

$$I = I_{sh} + I_d, \tag{2}$$

where $I_{sh}$ — the current through the shunt, $I_d$ — the current through the sample. A ratio of distribution of the currents depends on the ratio $R_p/R_{sh}$ in accordance with the expression (3):

$$\frac{I_d}{I_{sh}} = \frac{R_{sh}}{R_p}, \tag{3}$$

where $I_c$ — the true critical current of the sample. This expression shall be understood as follows: if $R_p = 0$, then the entire current will flow through the sample until reaching $I_c^{sh} = I_c$. However, when $R_p > 0$, the circuit will operate as a current splitter and a portion of the current will be transmitted through the shunt, which is why or achievement of the current in the sample, which is equal to $I_c$, the higher current will be required ($I > I_c$). Thus, in order to calculate the true critical current of the sample, it is necessary to use the expression

$$I_c = \frac{I_c^{sh}}{(1 + R_p/R_{sh})}. \tag{4}$$

From the measured current $I_c^{sh}$ for the samples *A1*–*A8*, according to the expression (4), we have obtained the value of the critical current $I_c$, which varies from 29 to $5\,\mu\text{A}$ at the temperature of 2.7 K (see Table). Let us compare the obtained critical current with the maximum possible depairing current. The obtained ratio of the critical current to the maximum possible one $I_c(T)/I_{dep}(T)$ is 0.5–0.87. It should be noted that both the samples demonstrate low readings of $I_c(T)/I_{dep}(T) \sim 0.5$. We suggest that reduction of the critical current in the NbN SMSPD can be related to a polycrystalline structure of the material. Due to crystallinity of this material, the superconducting properties of the films are sensitive to various defects of the substrate, which can result in origination of local defects of the film and removal of the critical current from $I_{dep}$. Nevertheless, the most detectors satisfy the condition $I_c(T)/I_{dep}(T) > 0.7$, at which origination of the single-photon response of SMSPD is expected [20]. A ratio of the potentially suitable detectors is 75 % of the eight equivalent samples. The maximum value of $I_c(T)/I_{dep}(T)$ is 0.87 at the temperature of 2.7 K. It was possible to achieve such a high index due to the design that prevents the flowing-current crowding effect.

Main parameters of the studied detectors

| Sample number | $I_c^{sh}$, $\mu$A | $R_p$, $\Omega$ | $I_c$, $\mu$A | $T$, K | $I_c(T)/I_{dep}(T)$ |
|---|---|---|---|---|---|
| *A1* | 71.4 | 20 | 44.2 | 2.7 | 0.75 |
| *A2* | 43 | 1.4 | 41.1 | 2.7 | 0.7 |
| *A3* | 60 | 9.7 | 46.3 | 2.7 | 0.79 |
| *A4* | 46 | 10 | 32 | 2.7 | 0.54 |
| *A5* | 55 | 2.5 | 50.8 | 2.7 | 0.87 |
| *A6* | 48.2 | 0.5 | 47.6 | 2.7 | 0.8 |
| *A7* | 49 | 1.6 | 46.7 | 2.7 | 0.8 |
| *A8* | 40.5 | 13.3 | 28.8 | 2.7 | 0.49 |

Note. In respective columns from left to right the table shows the sample number, $I_c^{sh}$ — the value of the critical current, which is experimentally obtained for the sample with the shunt, $R_p$ — the residual resistance of the superconductor, $I_c$ — the critical current of the superconductor, which is obtained from the expression (4), $T$ — the basic temperature of the measurements, $I_c(T)/I_{dep}(T)$ — the ratio of the critical current to the depairing current $I_{dep}$, which are taken at the basic temperature.

## Conclusions

We have designed the large-area multi-element superconducting single-photon NbN detector. The width of the stripes of each element is $0.5\,\mu$m, which is why these detectors can be classified as the superconducting detectors with the micron-wide stripe (SMSPD, Superconducting microwire single-photon detector). Smooth bends of the superconducting stripes and brodenings prevent the flowing-current crowding effect. Thanks to this, in 75% of the studied samples the value of the critical current to the depairing current $I_c(T)/I_{dep}(T)$ is close or even exceeds 0.7 at the temperature of 2.7 K, thereby indicating suitability of these samples as potential single-photon detectors. The active area size of the entire device is $45 \times 50\,\mu$m, which is suitable for matching with the multi-mode optical fiber. The obtained results show that our large-area multi-element detector has an advantage in the filling factor as compared to the large-area detectors based on the nanowire single-photon superconducting detectors (SNSPD) and has a big potential for further work dedicated to designing the large-area multi-element detector. Future work will be aimed at studying the single-photon response, the manufactured multi-element superconducting single-photon NbN detector and selecting the optimal shunt resistance.

### Funding

The work of designing and manufacturing the superconducting devices was supported by the grant from the Russian Science Foundation № 24-72-10105 and the volt-ampere characteristics were experimentally studied within the framework of the Fundamental Research Program of the HSE University in 2025

### Conflict of interest

The authors declare that they have no conflict of interest.

## References

[1] G.N. Goltsman, O. Okunev, G. Chulkova, A. Lipatov, A. Semenov, K. Smirnov, B. Voronov, A. Dzardanov, C. Williams, R. Sobolewski. Appl. Phys. Lett., **79** (6), 705 (2001). DOI: 10.1063/1.1388868

[2] G. Goltsman, A. Korneev, A. Divochiy, O. Minaeva, M. Tarkhov, N. Kaurova, V. Seleznev, B. Voronov, O. Okunev, A. Antipov, K. Smirnov, Yu. Vachtomin, I. Milostnaya, G. Chulkova. J. Modern Optics, **56** (15), 1670 (2009). DOI: 10.1080/09500340903277750

[3] B.A. Korzh, Q.-Y. Zhao, S. Frasca, J.P. Allmaras, T.M. Autry, E.A. Bersin, M. Colangelo, G.M. Crouch, A.E. Dane, T. Gerrits, F. Marsili, G. Moody, E. Ramirez, J.D. Rezac, M.J. Stevens, E.E. Wollman, D. Zhu, P.D. Hale, K.L. Silverman, R.P. Mirin, S.W. Nam, M.D. Shaw, K.K. Berggren. Nat. Photonics, **14**, 250 (2020). DOI: 10.1038/s41566-020-0589-x

[4] I.E. Zadeh, J.W.N. Los, R.B.M. Gourgues, J. Chang, A.W. Elshaari, J.R. Zichi, Y.J. van Staaden, J.P.E. Swens, N. Kalhor, A. Guardiani, Y. Meng, K. Zou, S. Dobrovolskiy, A.W. Fognini, D.R. Schaart, D. Dalacu, P.J. Poole, M.E. Reimer, X. Hu, S.F. Pereira, V. Zwiller, S.N. Dorenbos. ACS Photonics, 7, 1780 (2020). DOI: 10.1021/acsphotonics.0c00433

[5] J. Chiles, I. Charaev, R. Lasenby, M. Baryakhtar, J. Huang, A. Roshko, G. Burton, M. Colangelo, K. Van Tilburg, A. Arvanitaki, S.W. Nam, K.K. Berggren. Phys. Rev. Lett., **128** (23), 231802 (2022). DOI: https://doi.org/10.1103/PhysRevLett.128.231802

[6] S. Wang, Z.Q. Yin, D.Y. He, W. Chen, R.Q. Wang, P. Ye, Y. Zhou, G.J. Fan-Yuan, F.X. Wang, W. Chen, Y.G. Zhu, P.V. Morozov, A.V. Divochiy, Z. Zhou, G.C. Guo, Z.F. Han. Nature Photonics, **16** (2), 154 (2022). DOI: 10.1038/s41566-021-00928-2

[7] Y. Hochberg, I. Charaev, S.W. Nam, V. Verma, M. Colangelo, K.K. Berggren. Phys. Rev. Lett., **123** (15), 151802 (2019). DOI: https://doi.org/10.1103/PhysRevLett.123.151802

[8] F. Xia, M. Gevers, A. Fognini, A.T. Mok, B. Li, N. Akbari, I.E. Zadeh, J.Q. Dregely, C. Xu. ACS Photonics, **8** (9), 2800 (2021). DOI: https://doi.org/10.1364/CLEO_AT.2021.AM3C.6

[9] Y. Guan, H. Li, L. Xue, R. Yin, L. Zhang, H. Wang, G. Zhu, L. Kang, J. Chen, P. Wu. Opt. Laser Eng., **156**, 107102 (2022). DOI: https://doi.org/10.1016/j.optlaseng.2022.107102

[10] E.E. Wollman, J.P. Allmaras, A.D. Beyer, B. Korzh, M.C. Runyan, L. Narváez, W.H. Farr, F. Marsili, R.M. Briggs, G.J. Miles, M.D. Shaw. Opt. Express, **32** (27), 48185 (2024). DOI: https://doi.org/10.1364/OE.541425

[11] S. Steinhauer, S. Gyger, V. Zwiller. Appl. Phys. Lett., **118** (10), 100501 (2021). DOI: https://doi.org/10.1063/5.0044057

[12] J. Huang, W. Zhang, L. You, C. Zhang, C. Lv, Y. Wang, X. Liu, H. Li, Z. Wang. Supercond. Sci. Technol., **31** (7), 074001 (2018). DOI: 10.1088/1361-6668/aac180

[13] I. Craiciu, B. Korzh, A.D. Beyer, A. Mueller, J.P. Allmaras, L. Narváez, M. Spiropulu, B. Bumble, T. Lehner, E.E. Wollman, M.D. Shaw. Optica, **10** (2), 183 (2023). DOI: https://doi.org/10.48550/arXiv.2210.11644

[14] W. Zhang, J. Huang, W. Zhang, L. You, C. Lv, L. Zhang, H. Li, Z. Wang, X. Xie. IEEE Transactions Appl. Superconductivity, **29** (5), 1 (2019). DOI: 10.1109/TASC.2019.2895621

[15] L. Stasi, T. Taher, G.V. Resta, H. Zbinden, R. Thew, F. Bussières. arXiv preprint arXiv:2406.15312 (2024)

[16] G.V. Resta, L. Stasi, M. Perrenoud, S. El-Khoury, T. Brydges, R. Thew, H. Zbinden, F. Bussières. Nano Lett., **23** (13), 6018 (2023). DOI: https://doi.org/10.1021/acs.nanolett.3c01228

[17] F. Grünenfelder, A. Boaron, M. Perrenoud, G.V. Resta, D. Rusca, C. Barreiro, R. Houlmann, R. Sax, L. Stasi, S. El-Khoury, E. Hänggi, N. Bosshard, F. Bussiéres, H. Zbinden. Nature Photonics, **17**, 422 (2023). DOI: https://doi.org/10.1038/s41566-023-01168-2

[18] C. Peña, C. Wang, S. Xie, A. Bornheim, M. Barría, C.S. Martín, V. Vega, A. Apresyan, E. Knehr, B. Korzh, L. Narváez, S. Patel, M. Shaw, M. Spiropulu. arXiv preprint arXiv:2410.00251 (2024).

[19] M. Perrenoud, M. Caloz, E. Amri, C. Autebert, C. Schünenberger, H. Zbinden, F. Bussières. Supercond. Sci. Technol., **34** (2), 024002 (2021).

[20] D.Yu. Vodolazov. Phys. Rev. Appl., **7**, 034014 (2017). DOI: https://doi.org/10.1103/PhysRevApplied.7.034014

[21] Y. Korneeva, D.Yu. Vodolazov, A.V. Semenov, I. Florya, N. Simonov, E. Baeva, A.A. Korneev, G.N. Goltsman, T.M. Klapwijk. Phys. Rev. Appl., **9** (6), 064037 (2018). DOI: https://doi.org/10.1103/PhysRevApplied.9.064037
[22] G.Z. Xu, W.J. Zhang, L.X. You, Y.Z. Wang, J.M. Xiong, D.H. Fan, L. Wu, H.Q. Yu, H. Li, Z. Wang. Opt. Express, **31** (10), 16348 (2023). DOI: 10.1364/OE.487024
[23] J.S. Luskin, E. Schmidt, B. Korzh, A.D. Beyer, B. Bumble, J.P. Allmaras, A.B. Walter, E.E. Wollman, L. Narváez, V.B. Verma, S.W. Nam, I. Charaev, M. Colangelo, K.K. Berggren, C. Peña, M. Spiropulu, M.G. Sciveres, S. Derenzo, M.D. Shaw. Appl. Phys. Lett., **122** (24), 243506 (2024). DOI: https://doi.org/10.1063/5.0150282
[24] A.J. Kerman, J.K.W. Yang, R.J. Molnar, E.A. Dauler, K.K. Berggren. Phys. Rev. B–Condensed Matter Mater. Phys., **79** (10), 100509 (2009). DOI: https://doi.org/10.1103/PhysRevB.79.100509
[25] M.W. Brenner, D. Roy, N. Shah, A. Bezryadin. Phys. Rev. B–Condensed Matter Mater. Phys., **85** (22), 224507 (2012). DOI: https://doi.org/10.1103/PhysRevB.85.224507
[26] H.L. Hortensius, E.F.C. Driessen, T.M. Klapwijk, K.K. Berggren, J.R. Clem. Appl. Phys. Lett., **100** (18), 182602 (2012). DOI: https://doi.org/10.1063/1.4711217
[27] Yu.P. Korneeva, N.N. Manova, M.A. Dryazgov, N.O. Simonov, Ph.I. Zolotov, A.A. Korneev. Supercond. Sci. Technol., **34** (8), 084001 (2021). DOI: 10.1088/1361-6668/ac0950
[28] J.R. Clem, V.G. Kogan. Phys. Rev. B, **86**, 174521 (2012). DOI: 10.1103/PhysRevB.86.174521
[29] A. Semenov, B. Günther, U. Böttger, H. Hübers, H. Bartolf, A. Engel, A. Schilling, K. Ilin, M. Siegel, R. Schneider, D. Gerthsen, N. Gippius. Phys. Rev. B, **80**, 054510 (2009). DOI: https://doi.org/10.1103/PhysRevB.80.054510

*Translated by M.Shevelev*